

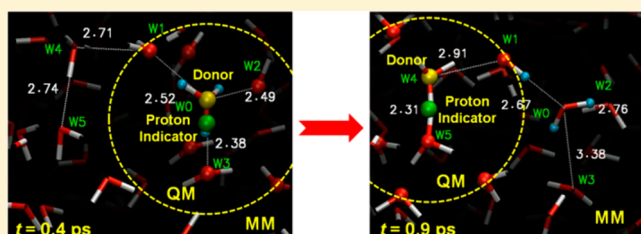
Adaptive-Partitioning QM/MM for Molecular Dynamics Simulations: 4. Proton Hopping in Bulk Water

Soroosh Pezeshki and Hai Lin*

Chemistry Department, University of Colorado Denver, Denver, Colorado 80217-3364, United States

S Supporting Information

ABSTRACT: By reclassifying atoms as QM or MM on-the-fly, adaptive QM/MM dynamics simulations can utilize small QM subsystems whose locations and contents are continuously and automatically updated. Although adaptive QM/MM has been applied in studies of a variety of ions, dynamics simulations of a hydrated proton in bulk water remain a challenge. The difficulty arises from the need to transfer structural features (the covalent and hydrogen bonding networks) via the Grotthuss mechanism instead of the given proton. One must therefore identify an appropriate reference point from which the QM subsystem can be positioned that continuously follows the structural variations as the proton hops. To solve this problem, we propose a proton indicator that serves as the needed reference point. The location of the proton indicator varies smoothly from the hydronium oxygen in the resting (Eigen) state to the shared proton in the transition (Zundel) state. The algorithm is implemented in the framework of a modified permuted adaptive-partitioning QM/MM. As a proof of concept, we simulate an excess proton solvated in bulk water, where the QM subsystem is defined as a sphere of 4.0 Å radius centered at the proton indicator. We find that the use of the proton indicator prevents abrupt changes in the location and contents of the QM subsystem. The new method yields reasonably good agreement in the proton solvation structure and in the proton transfer dynamics with previously reported conventional QM/MM dynamics simulations that employed a much larger QM subsystem (a sphere of 12 Å radius). Also, the results do not change significantly with respect to variations in the time step size (0.1 or 0.5 fs), truncation of the many-body expansion of the potential (from fifth to second order), and absence/presence of thermostat. The proton indicator combined with the modified permuted adaptive-partitioning scheme thus appears to be a useful tool for studying proton transfer in solution.



1. INTRODUCTION

Molecular dynamics (MD) simulations of proton transfer via the Grotthuss shuttling mechanism¹ have drawn much attention due to their importance in many life and industrial processes.² The mechanism requires dynamical reorganization of the covalent and hydrogen bonding network surrounding the hydrated proton, which may exist as a hydronium or Zundel ion. Although empirical molecular-mechanics (MM) force fields^{3–12} and multistate empirical valence bond (MS-EVB) models^{13–25} have been developed to describe water dissociation and applied to simulate proton hopping in bulk water; ideally, the bond breaking and forming processes are best described at the quantum-mechanics (QM) level of theory. Studies^{2,21,22,26–36} based on Car–Parrinello MD³⁷ have played a prominent role in this regard, where the potentials were computed on-the-fly at the level of density functional theory. Another set of QM studies were based on Born–Oppenheimer MD and employed semiempirical methods.^{38–47} Those calculations have provided valuable insights into the solvation structure and the transport mechanism of the hydrated proton.

A problem arises when performing MD simulations based on combined quantum-mechanical and molecular-mechanical (QM/MM)^{48–68} descriptions: which water molecules should be designated as QM? Intuitively, it is necessary to incorporate

the water molecules in the first solvation shell of the hydrated proton at the QM level. However, exchange of water molecules between the solvation shell and the bulk solvent is expected and can occur quickly. It is very difficult, if not impossible, to judge in advance which water molecule will move into the solvation shell and thus be assigned as QM. Moreover, because of the dynamical reorganization of the covalent and hydrogen bonding network, the identity of the hydrated proton can change, or “hop”, quickly from one site to another. Therefore, proton transfer may be hindered if the hydrated proton moves to the QM/MM boundary after an MD simulation has begun.

One simple solution to overcome the hurdle caused by the QM/MM boundary is to utilize a large localized QM subsystem. Because the QM subsystem is also called the primary subsystem for it being of primary interest to us, we denote the conventional QM/MM calculation with a large QM subsystem as QM/MM-LPS (meaning QM/MM-with-large-primary-subsystem). The QM or primary subsystem should be sufficiently large for the desired time scale of the MD simulation, such that the probability is negligibly small for the hydrated proton to move near the QM/MM boundary. A large

Received: November 14, 2014

QM subsystem also likely keeps the exchange of QM and MM solvent molecules far away from the hydrated proton. In practice, the exchange of QM and MM solvent molecules may even be prohibited (e.g., by applying restraining potentials to certain water molecules near the QM/MM boundary). This strategy is straightforward and relatively easy to implement. For example, a droplet model has recently been adopted in QM/MM simulations of proton transfer in bulk solvent by Wu et al.⁴⁵ This droplet model separated the water molecules into two layers. The inner layer was a sphere of $R_{\text{inner}} = 12 \text{ \AA}$ that contained a hydronium ion at the center and 213 water molecules surrounding the hydronium ion, all of which were treated by QM and were free to move. The 1269 water molecules in the outer layer of $R_{\text{inner}} < R \leq R_{\text{system}} = 22 \text{ \AA}$ were treated by MM and were subjected to harmonic potentials that restrained the oxygen atoms to their original positions. In a series of MD simulations, each of which lasted for 22 ps, the hydrated proton never moved near the QM/MM boundary, and very few water molecules diffused from the first (QM) layer into the second (MM) layer. Although the QM/MM-LPS model worked well for the reported MD simulations, the drawbacks were also apparent: the large QM subsystem makes the calculations expensive, and the finite-size QM subsystem will eventually run into trouble in longer simulations.

Adaptive QM/MM^{69–86} offers another promising solution to overcome issues with static barriers by permitting the on-the-fly, automated reclassification of atoms/groups as part of the QM or MM subsystem. Consequently, the QM subsystem is updated as needed during the MD simulations without human interference. The finite-size QM subsystem becomes, in a sense, infinite and can in principle sustain MD simulations that last forever. Furthermore, one can minimize the size of the QM subsystem to keep the computational cost low. Applying the adaptive QM/MM algorithms to model proton transfer in bulk water is therefore highly attractive. However, existing adaptive algorithms in the literature^{69–84} cannot meet the challenge of proton transfer because they all require a preselected atom or the center of mass of a preselected set of atoms to serve as the center of a sphere that defines the QM subsystem. When modeling “ordinary” ions, such as Cl^- and Na^+ , the QM subsystem center can be conveniently set to the ion, or if the ion is polyatomic, to a designated atomic center or the center of mass of the ion. (In this paper, unless otherwise noted, an ion is referred to as an ordinary ion.) For proton transfer, however, what is being transferred is the structural features of the covalent and hydrogen bonding network, not the given proton. Therefore, one must find another way that reflects the changes in the bonding network to update the location and contents of the QM subsystem on-the-fly as the excess proton hops. Moreover, the updates must be as smooth and continuous as possible to avoid discontinuities in the MD simulations. Any new adaptive QM/MM scheme for proton transfer should meet these two requirements.

In the present contribution, we report a new implementation of the permuted adaptive-partitioning (PAP) QM/MM^{72,77,84} scheme for MD simulations of proton transfer in bulk water. Initially developed for the study of ions and molecules solvated in solvent,⁷² PAP schemes have recently been extended to protein simulations. Progress includes a method for on-the-fly relocation of the QM/MM boundaries that pass through covalent bonds⁷⁷ and a method for treating solvent molecules entering and leaving protein binding sites.⁸⁴ The present study extends the PAP scheme to describe proton hopping in bulk

water. The new treatment employs an explicit proton indicator whose coordinates are updated on-the-fly according to the ever-changing structural features of the bonding network around the hydrated proton. The position of the proton indicator represents the approximate location of the excess proton. With the QM-subsystem centered at the proton indicator, we were able for the first time to carry out adaptive QM/MM simulations for a hydrated proton. The new PAP scheme will be benchmarked by the QM/MM-LPS calculations that have been reported previously.⁴⁵ Because our aim in this proof-of-concept paper is to examine the applicability of the proton indicator in adaptive QM/MM simulations, agreements with experimental results have not been pursued.

II. METHODOLOGY

II.A. Permuted Adaptive-Partitioning QM/MM. Reclassifying an atom or molecule as QM or MM on-the-fly faces the challenge that the energy and forces may change abruptly, which leads to numerical instabilities as well as ambiguities in the interpretation of results. To circumvent this problem, an adaptive algorithm usually inserts a buffer zone between the QM and MM subsystems (Figure 1). The QM subsystem is

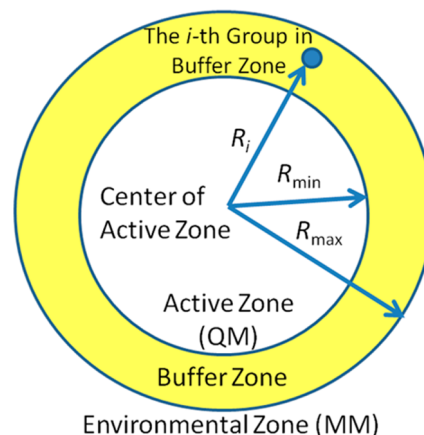


Figure 1. Schematics of the active zone (modeled by QM), buffer zone (dual QM and MM identities), and environmental zone (modeled by MM) in adaptive-partitioning QM/MM calculations. A group is in the buffer zone if its distance to the active-zone center is between two preset thresholds R_{min} and R_{max} .

often defined as a sphere of radius R_{min} centered at a given atom or the center of mass of a set of preselected atoms. The buffer zone is defined by $R_{\text{min}} < R \leq R_{\text{max}}$ where R is the distance away from the QM-subsystem center, and R_{max} is the radius of the sphere where the buffer zone meets the MM subsystem (defined by $R > R_{\text{max}}$). In adaptive QM/MM, the QM subsystem is often called the active zone, and the MM subsystem is called the environmental zone. The atoms and molecules in the buffer zone are known as the buffer groups, and they have dual QM and MM characteristics. Smoothing functions are applied to the energy or the forces, which eliminate or reduce discontinuities in these quantities when groups are exchanged between the QM and MM subsystems.

Two adaptive-partitioning (AP) QM/MM schemes have been proposed.⁷² One of the algorithms, permuted adaptive-partitioning (PAP), was demonstrated to offer superior numerical stability.^{72,77} Briefly, in the PAP scheme, the potential energy of the system with N buffer groups is defined in a many-body expansion manner

$$\begin{aligned}
 V = V^A &+ \sum_{i=1}^N P_i(V_i^A - V^A) \\
 &+ \sum_{i=1}^{N-1} \sum_{j=i+1}^N P_i P_j (V_{ij}^A - [V^A + \sum_{r=i,j} (V_r^A - V^A)]) \\
 &+ \sum_{i=1}^{N-2} \sum_{j=i+1}^{N-1} \sum_{k=j+1}^N P_i P_j P_k (V_{ijk}^A - (V^A + \sum_{r=i,j,k} (V_r^A - V^A))) \\
 &+ \sum_{(p,q)=(i,j),(i,k),(j,k)} (V_{p,q}^A - (V^A + \sum_{r=(p,q)} (V_r^A - V^A))) + \dots
 \end{aligned} \quad (1)$$

where V^A is the energy determined with the groups in the active zone at the QM level, V_i^A with all active-zone groups and the i -th buffer-zone group at the QM level, V_{ij}^A with all active-zone groups, the i -th buffer-zone group, and the j -th buffer-zone group at the QM level, ... $V_{1,2,\dots,N}^A$ with all active-zone groups and all N buffer-zone groups at the QM level, and P_i is the smoothing function of the i -th buffer-zone group in terms of the dimensionless reduced radial coordinate α_i

$$\alpha_i = \frac{R_i - R_{\min}}{R_{\max} - R_{\min}} \quad (2)$$

$$P_i(\alpha_i) = \begin{cases} 0 & 1 \leq \alpha_i \\ -6\alpha_i^5 + 15\alpha_i^4 - 10\alpha_i^3 + 1 & 0 \leq \alpha_i < 1 \\ 1 & \alpha_i < 0 \end{cases} \quad (3)$$

where R_i is the distance from the active-zone center to the i -th buffer-zone group. Because the energy contributions of the terms in the series in eq 1 decrease rapidly, truncation of the series is recommended to reduce the number of embedded-QM calculations. The resulting small discontinuities in the energy and derivatives are controllable and have been shown to be insignificant if the series is truncated at the fifth order^{72,77,84} (i.e., at no point in time is a QM/MM calculation performed with more than the active zone and 5 buffer zone groups treated at the QM level).

A modification to the original PAP schemes was recently proposed, where the extra forces due to the smoothing functions were deleted in the propagation of trajectories.⁸⁴ Those extra forces may cause artifacts if they are not negligible when compared with the “real” forces in the QM and MM calculations.⁸⁴ The removal of the extra forces does not cause violation of Newton’s Third Law of Motion, and the modified PAP (denoted as mPAP) scheme still conserves the momentum. However, the energy is not defined, because the modified forces cannot be expressed as exact differentials of a potential. The removal of the extra forces is equivalent to applying external forces to the involved atoms to cancel out those extra forces. The mPAP method describes a non-Hamiltonian system, which can be coupled to a thermostat so that NVT simulations can be performed. Just like in the original PAP scheme, the forces on all involved atoms are smoothed in the mPAP method. The present study is based on the mPAP scheme.

II.B. Proton Indicator. In the present contribution, the active-zone center was set to a proton indicator (I), whose position gives the approximate location of the excess proton (Figure 2). The indicator has the following properties:

(1) It indicates the approximate location of the hydrated excess proton. In the limit of Eigen ion H_3O_4^+ , its position

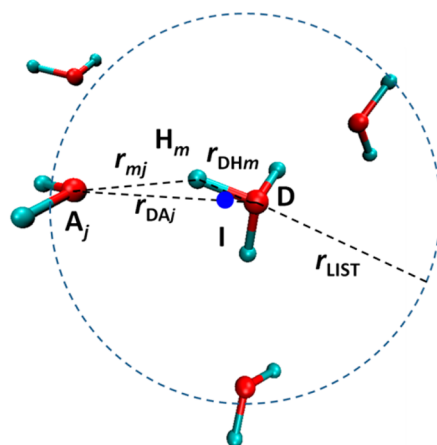


Figure 2. Illustration of the proton indicator (I), whose location is determined jointly by the positions of the donor oxygen atom (D), donor hydrogen atoms (H_m), and possible acceptor oxygen atoms (A_j). The potential acceptors are the oxygen atoms of nearby water molecules whose distances from the donor oxygen atom (r_{DA_j}) are smaller than a predefined enlisting threshold r_{LIST} . The distance between D and A_j is r_{DA_j} , and between D and H_m is r_{DH_m} . The hydronium ion and water molecule are shown in ball and stick models with oxygen in red and hydrogen in cyan. The water indicator is shown as a blue sphere lying in the line connecting D and A_j .

superimposes with donor D (the oxygen atom of the hydronium ion), whereas in the limit of the Zundel ion H_5O_2^+ , its position superimposes with the shared hydrogen atom at the midpoint between the two oxygen atoms of the Zundel ion. Furthermore, when the structure varies between the two limits, the indicator’s position should change accordingly.

(2) Its coordinates are a function of the coordinates of the donor D, the hydrogen atoms H_m ($m = 1, 2$, and 3) bonded to D, and the possible acceptors A_j ($j = 1, 2, \dots$). The possible acceptors are the oxygen atoms of the water molecules within a threshold distance r_{LIST} from D. There are certainly other choices, but this one seems to be convenient.

(3) At any given time, the most likely acceptor among all possible acceptors is denoted A. (The criteria of determining A will be discussed later.) When proton transfer occurs, A and D switch statuses, and the list of A_j is updated. Those changes should lead to minimal perturbation of the indicator’s position, which is necessary for a smooth change in the indicator’s position.

(4) The position of the indicator is insensitive to the vibrations of the D– H_m bonds near the equilibrium.

We determined the indicator’s position according to the following equations

$$\mathbf{X}_I = \frac{1}{g_I} \left(\mathbf{X}_D + \sum_{j=1}^J \sum_{m=1}^M g(\rho_{mj}) \mathbf{X}_{\text{A}_j} \right) \quad (4)$$

$$g_I = 1 + \sum_{j=1}^J \sum_{m=1}^M g(\rho_{mj}) \quad (5)$$

The indicator’s position is given by a weighted average of the coordinates of the donor and all possible acceptors, where g_I is the normalization factor. Here, \mathbf{X}_I , \mathbf{X}_D , and \mathbf{X}_{A_j} are the Cartesian coordinates of the indicator, donor, and j -th possible acceptor,

respectively, M is the total number of hydrogen atoms H_m bonded to the donor, J is the total number of the possible acceptors, and $g(\rho_{mj})$ is a weight function that depends on ρ_{mj} , a ratio indicating how close H_m is to donor D versus to a possible acceptor A_j . As done in ref 87, we define ρ_{mj} using projected donor–acceptor vectors

$$\rho_{mj} = \frac{\mathbf{r}_{DH_m} \mathbf{r}_{DA_j}}{|\mathbf{r}_{DA_j}|^2} \quad (6)$$

where $\mathbf{r}_{DH_m} = \mathbf{X}_{H_m} - \mathbf{X}_D$ and $\mathbf{r}_{DA_j} = \mathbf{X}_{A_j} - \mathbf{X}_D$. The gradients of ρ_{mj} with respect to \mathbf{X}_{H_m} , \mathbf{X}_{A_j} , and \mathbf{X}_D are given in the Supporting Information.

The requirements of the weight functions are as follows: First, the value of weight function $g(\rho_{mj})$ should be 1 at $\rho_{mj} = 0.5$, which corresponds to equal sharing of a proton between the two waters in the Zundel structure. Second, $g(\rho_{mj})$ must fall quickly to 0 as ρ_{mj} decreases approaching $\rho_{mj}^0 = (r_{DH}^0/r_{LIST})$, where $r_{DH}^0 = 1.00$ Å is a parameter taken to be slightly larger than the equilibrium OH bond length in the hydronium ion. For $\rho_{mj} < \rho_{mj}^0$, $g(\rho_{mj}) = 0$. The smooth and fast decrease of $g(\rho_{mj})$ to 0 ensures that the indicator position is dominated by donor D and the most likely acceptor A_j , bringing minimal changes in \mathbf{X}_i when D and A switch. In principle, because the identities of donor and acceptor switch at $\rho_{mj} = 0.5$, ρ_{mj} should never exceed 0.5. In practice, however, the value of ρ_{mj} may sometimes go slightly above 0.5 during trajectory propagation due to finite time step sizes; we therefore require that $g(\rho_{mj}) = 1$ for $\rho_{mj} > 0.5$. The simulations that use proton indicator as defined in this work are not time-reversible.

We tested various weight functions for $g(\rho_{mj})$, including polynomials, exponential functions, and Gaussian functions. An exponential function or Gaussian function does not reach exactly 0 at $\rho_{mj} = \rho_{mj}^0$, but it can be parametrized such that the values are negligibly small (e.g., 10^{-8}) at that point. More details about the tested weight functions are provided in the Supporting Information. Among those tested functions, the one that worked the best is a fifth order polynomial that depends on reduced variable x

$$g(x) = \begin{cases} 0 & \text{if } 1 \leq x \\ -6x^5 + 15x^4 - 10x^3 + 1 & \text{if } 0 \leq x < 1 \\ 1 & \text{if } x < 0 \end{cases} \quad (7)$$

$$x = x(\rho_{mj}) = 1 - \frac{\rho_{mj} - \rho_{mj}^0}{0.5 - \rho_{mj}^0} \quad (8)$$

It follows that for $\rho_{mj} \geq 0.5$, then $x \leq 0$ and $g(x) = 1$ and that for $\rho_{mj} \leq \rho_{mj}^0$, then $x \geq 1$ and $g(x) = 0$. The gradients of the weight function go smoothly toward 0 as ρ_{mj} approaches either ρ_{mj}^0 or 0.5. We employed this polynomial weight function in the reported simulations.

III. COMPUTATION

The QM/MM dynamics simulations using the mPAP scheme employed a model with periodic boundary conditions. The primary simulation cell contains one hydronium ion embedded in a box of 1435 water molecules that was pre-equilibrated for 100 ps at the MM level using the TIP3P⁸⁸ water model, giving rise to 4309 atoms in total. The fixed dimensions of the primary water box are $35.2 \times 35.2 \times 35.2$ Å³, and the density is 1.0 g/

mL. The hydronium ion was placed at the center of the box. A uniform charge background was assumed for charge neutrality. The QM/MM calculations were carried out at the OM3n/TIP3P level, where OM3n is a recently reparameterized semiempirical Hamiltonian specifically designed for proton transfer in bulk water.⁴⁵ The OM3n Hamiltonian has been found to yield excellent results for many structural and dynamic properties of water and of hydrated proton in a recent conventional QM/MM-LPS study, including a small but finite barrier of 0.1–0.2 kcal/mol in the potential of mean force for proton transfer in bulk water,⁴⁵ which is in remarkable agreement with ab initio path-integral simulations (0.15 kcal/mol)^{28,29} that include the quantum fluctuations of all nuclei. The high computational efficiency and good accuracy of OM3n made it an excellent choice for the QM calculations in this work. For simplicity, we have chosen the mechanical embedding scheme. To avoid discontinuities in the potential when the donor and acceptor switch statuses, we assigned the hydronium hydrogen the same MM parameters as the water hydrogen. Likewise, the hydronium oxygen and water oxygen were given the same MM parameters. (Such a practice has previously been used in the QM/MM-LPS calculations.⁴⁵) The treatments lead to an overall charge of the hydronium of +0.417 e rather than +1 e. Although the treatment is not perfect, it avoids abrupt changes in the potential.

The mPAP calculations employed a buffer zone of 0.5 Å thickness with $R_{\min} = 4.0$ Å and $R_{\max} = 4.5$ Å. The size of the active zone was chosen such that the QM subsystem contains the first solvation shell of the hydrated proton and is close to the smallest active zone that one could reasonably construct for simulating proton hopping in bulk water. With such a small QM subsystem, it is unlikely that the mPAP calculations will reproduce all properties obtained by full-QM or QM/MM-LPS calculations, where different levels of treatment are applied to the interactions between the small number of species in the first solvation shell and the water molecules in the bulk.

Each water molecule was considered as one group in the adaptive partitioning, and the potentials $V_{1,2,\dots}^A$ are aligned such that they agree with each other when the water molecules are separated infinitely far away from each other. The threshold distance r_{LIST} for bookkeeping of the possible acceptors was set to 2.60 Å so that usually all three water molecules in the Eigen ion were enlisted as possible acceptors. The topology (bond connectivity) of the model system was updated each step. The TIP3P water molecules were flexible in the simulations, as in the previous QM/MM-LPS calculations.⁴⁵ The system was coupled to a Berendsen thermostat⁸⁹ at 298.15 K with a coupling constant of 4 fs. A cutoff of 14 Å was used for the nonbonded interactions with a linear tapering switched on at 13 Å. Three independent trajectories, each 15 ps long, were propagated with a time step size of 0.5 fs and were saved every 20 steps. These trajectories are denoted Long₁, Long₂, and Long₃ (Table S1 in the Supporting Information).

We have carried out additional sets of calculations of shorter simulation time to explore how the simulations are affected by computational setups, such as truncation of the many-body expansion of potential, time step size, thermostat, and so forth. These additional sets of calculations are denoted Add-a to Add-e (Table S1 in the Supporting Information), where each trajectory was propagated for 5 ps employing a step size of 0.5 fs and was saved every 20 steps, unless otherwise indicated. A brief description of the additional calculations is given below.

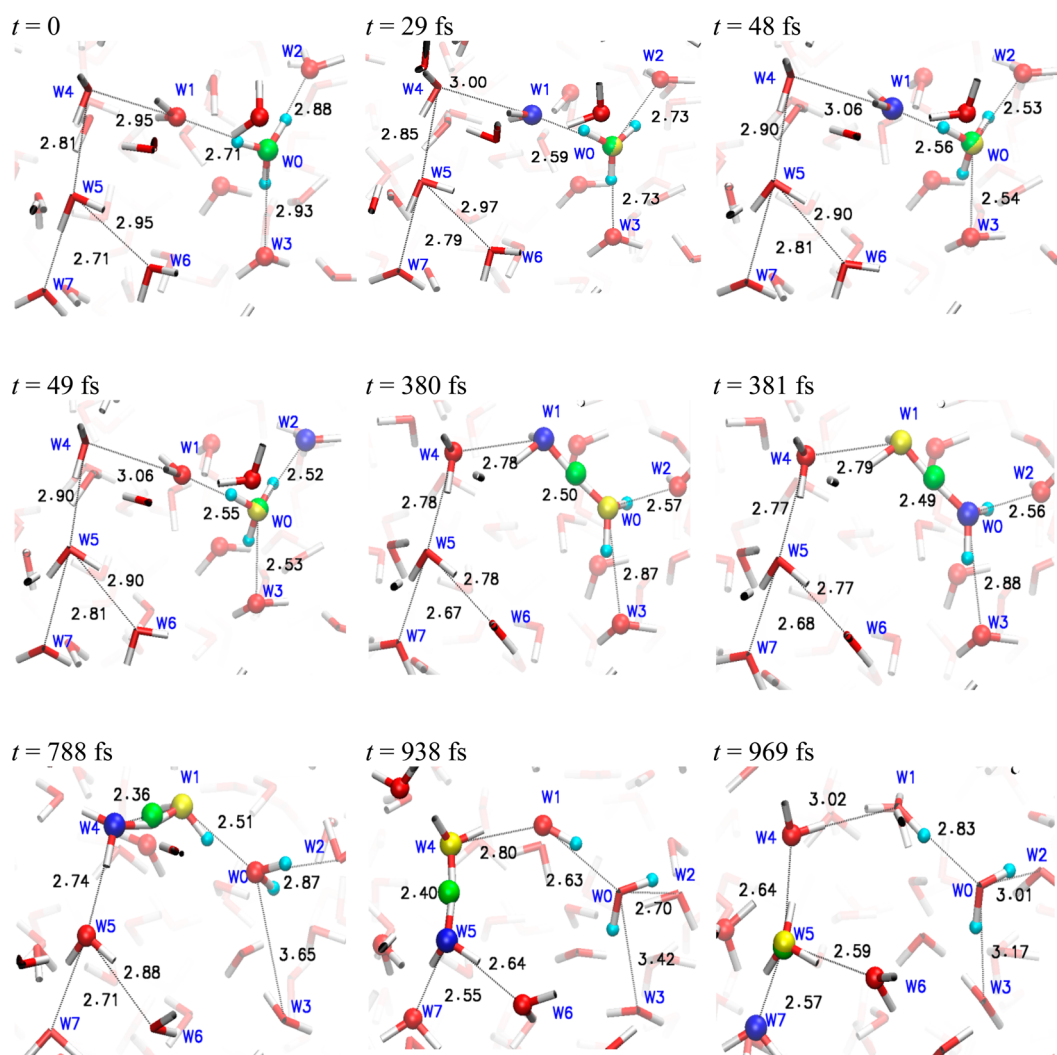


Figure 3. Snapshots from the sample short trajectory Add-a₁. Water molecules are represented by bonds (O, red; H, white), donor D as a yellow sphere, acceptor A as a blue sphere, proton indicator as a green sphere, and the H atoms belonged to the original hydronium ion (W0) as cyan spheres. The active zone always contains D and A. If a water molecule is in the active zone at a given time, its oxygen is shown as a red sphere. Water molecules W1–W7 are involved in proton transfer during the simulation. Distances are in Å.

Add-a: To check whether the proton indicator indeed undergoes smooth transitions in the simulations, we generated 4 independent short trajectories, Add-a₁ to Add-a₄, each of which was 1 ps long and was saved every step. The saved trajectories were visually inspected in great detail.

Add-b: To check if truncation of the many-body expansion of potential (eq 1) at lower orders will significantly deteriorate the accuracy of the simulations, we performed simulations in which the expansions were truncated at fourth, third, and second orders. Two independent trajectories were generated for each of the truncation orders, leading to 6 trajectories in total.

Add-c: To explore the effect due to the time step size, we carried out two sets of simulations employing a step size of 0.1 fs, where the many-body expansion in eq 1 was truncated at fifth and third orders. Two trajectories were generated for each set of the simulations. The trajectories for the simulations with fifth-order truncation were 3.5 ps long.

Add-d: To examine the numerical stability of the simulation, we performed simulations without coupled thermostats. Two trajectories were generated.

Add-e: Simulations with larger active-zones of 6 and 8 Å were also attempted with the many-body expansion of potential

truncated at the third and second orders, respectively. Unfortunately, the computational cost of those simulations was too high (see Figure S2 in the Supporting Information) and only very short (2 and 1.5 ps, respectively) trajectories were obtained. These short trajectories were deemed unsuitable for quantitative analysis due to poor statistics.

All calculations were carried out using a new version of the QMMM⁹⁰ program, which calls TINKER,⁹¹ for the MM gradient calculations and MNDO⁹² for the QM gradient calculations. The QMMM program then combines the MM and QM gradients and propagates the QM/MM trajectory.

IV. RESULTS

IV.A. Proton Indicator as Active Zone Center. First, we took a look at the proton indicator. Visual inspection of all sample trajectories in the Add-a set of calculations confirmed that the proton indicator indeed moved smoothly in the simulations. As an example, a movie for one of the sample trajectories (Add-a₁) was provided in the Supporting Information. The movie shows that initially the excess proton stayed at the original hydronium ion W0. Around $t = 0.4$ ps, the

excess proton was shuttled back and forth quickly between W0 and nearby water molecule W1, which was hydrogen-bonded to W0; this kind of fast oscillatory movement between a pair of water molecules does not lead to proton hopping. The first occurrence of proton hopping through the Grotthuss mechanism (called the forward proton hopping) was observed at approximately $t = 0.8$ ps, when the identity of the donor switched to a third water molecule W4. The second forward hopping occurred at approximately $t = 0.95$ ps when the donor changed to W5.

Figure 3 shows a few snapshots taken from the sample Add- a_1 trajectory:

(1) At $t = 0$, all water molecules were beyond the r_{LIST} range, no acceptor was identified, and the proton indicator superimposed with the hydronium oxygen at W0. Clearly, this geometry corresponded to the Eigen structure. Besides W0, the active zone contained 5 water molecules, including the 3 water molecules (W1–W3) hydrogen-bonded to W0.

(2) After the simulation started, water molecules moved closer to W0, and the acceptor A was identified as W1 at $t = 28$ fs. Enlisting of the acceptor had negligible effects on the indicator's position, which was still superimposed with the W0 oxygen. There was one more water molecule in the active zone at this moment, leading to 6 QM water molecules besides W0.

(3) Between $t = 48$ and 49 fs, the acceptor switched from W1 to W2. However, the sudden change of acceptor identity brought an insignificant perturbation to the location of the indicator, which stayed close to the donor. The contents of the active zone did not change.

(4) The switch of the donor was exemplified by the two snapshots of $t = 380$ and 381 fs, where the donor jumped from W0 to W1. The sudden change of the donor's identity barely modified the indicator's position, which was superimposed almost completely with the proton shared by W0 and W1.

(5) The last three snapshots illustrated the forward hops of the proton from W1 to W4 and finally to W5. Note that the QM subsystem was updated along the way. For example, W0 was in the active zone at $t = 788$ fs but not anymore at $t = 938$ fs, and W1 also dropped out between $t = 938$ and 969 fs. At the same time, other water molecules entered the active zone. For example, W6 and W7 became QM groups once the donor was relocated to W4 and continued to stay in the QM subsystem after the proton hopped to W5.

The proton indicator's movements along with the geometry evolution demonstrated that the proton indicator followed the excess proton smoothly as the proton hopped with little perturbation due to the sudden changes in the donor and acceptor identities. Thus, the proton indicator provided a reasonable, though approximate, way to locate the position of the excess proton in transition, and it served well as the active-zone center in adaptive-partitioning QM/MM simulations.

The numbers of active and buffer groups versus simulation time are exemplified in Figure 4 (A and B) for short (Add- a_1) and long (Long- a_1) sample trajectories, respectively. The number of active groups fluctuated in Add- a_1 between 5 and 10 with an average of 6.7, and the buffer group number varied between 0 and 6 with an average of 2.0. The results for Long- a_1 were qualitatively similar with the average numbers of active and buffer groups being somewhat larger (8.6 and 3.0, respectively). Averaging over all three long (Long- a_1 to Long- a_3) trajectories, the numbers of active and buffer groups were 8.6 and 3.2, respectively. The relatively small numbers for the buffer groups were due to the small radius (4 Å) of the active zone in those

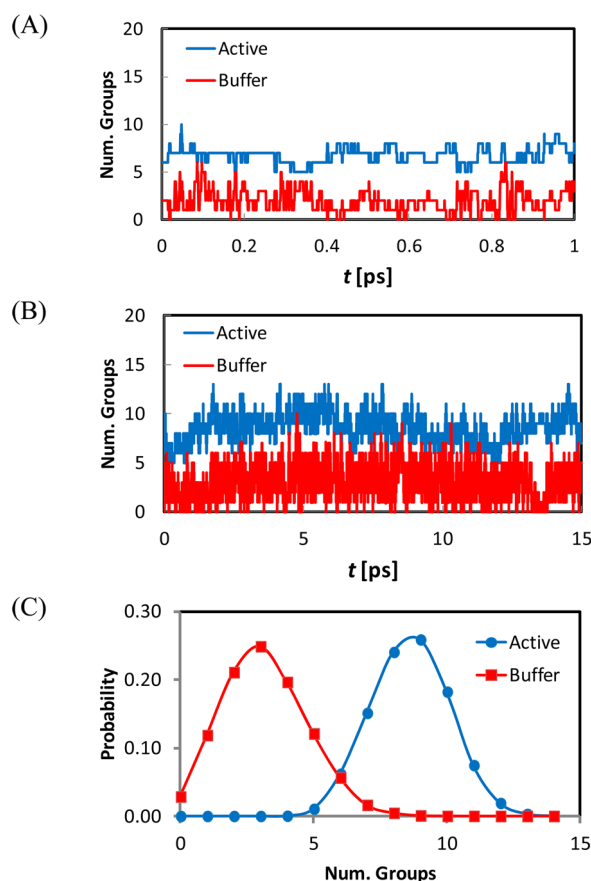


Figure 4. Number of active and buffer groups as a function of simulation time for (A) a short sample trajectory Add- a_1 and (B) a long sample trajectory Long- a_1 . (C) The probability distributions of the numbers of the active and buffer groups in the 45 ps combined trajectories of Long- a_1 , Long- a_2 , and Long- a_3 .

calculations. The probability distributions are given in Figure 4 (C) for the numbers of active and buffer groups based on the three long simulations. Both distributions resemble the bell shape of a Gaussian function.

IV.B. Solvation Structure of the Excess Proton. In Figure 5 (A), we compare the radial distribution functions (RDFs) $g_{\text{D-O}}(r)$ for the pair of the donor and the water oxygen between the mPAP-QM/MM and QM/MM-LPS⁴⁵ results. The mPAP RDF was computed using three long (Long- a_1 –Long- a_3) trajectories, and it resembles the LPS curve up to $r \approx 3.5$ Å. Note that to ease the comparison, we have scaled the RDF in the LPS calculations by a factor of ~ 1100 , which employed a droplet model rather than periodic boundary. Both mPAP and LPS $g_{\text{D-O}}(r)$ curves show one single nonsplit peak located at $r = 2.5$ Å. This peak corresponds to the first solvation shell of the donor (i.e., the 3 equiv water molecules surrounding the hydronium ion in the Eigen structure). For reasons that we discuss later, the agreements between mPAP and LPS are less satisfactory at larger r values. For example, the location of the first minimum in the mPAP curve is at $r = 3.4$ Å, slightly smaller than the 3.6 Å in the LPS plot.

The integrated coordination number (ICN) $n_{\text{D-O}}(r)$ curves are displayed in Figure S1 of the Supporting Information. In Figure S1 (A) in the Supporting Information, it is seen that the hydronium ion is surrounded by ~ 2 less water molecules in mPAP than in the LPS calculations and that this difference is introduced at approximately $r = 3$ Å. Although many factors

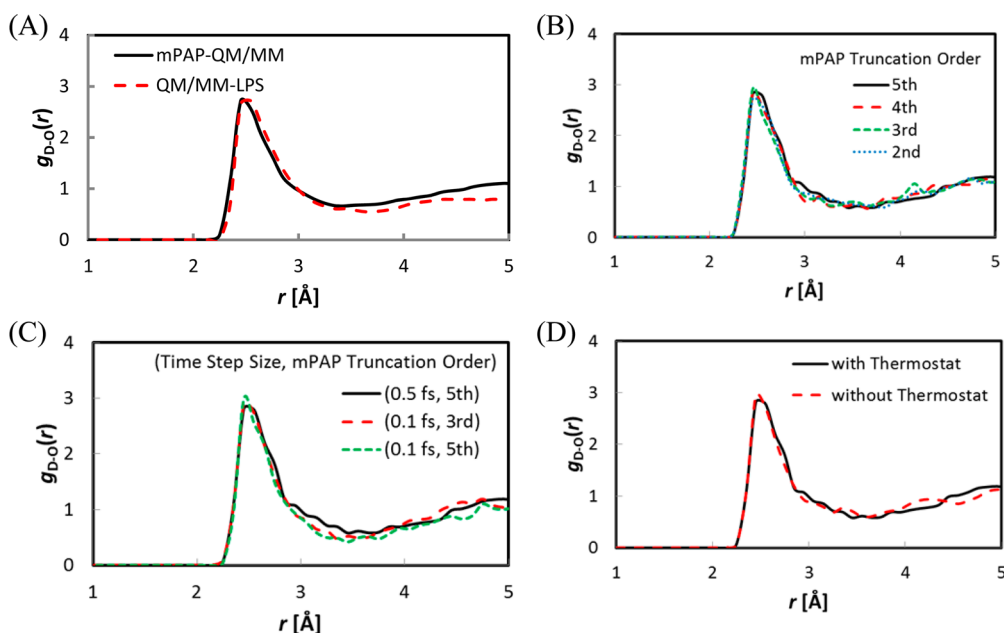


Figure 5. Radial distribution function (RDF) $g_{D-O}(r)$, where D is the donor and O the oxygen of water. (A) Comparison of the mPAP-QM/MM and QM/MM-LPS⁴⁵ results. The mPAP results are based on the 45 ps combined trajectories of Long₁, Long₂, and Long₃. Because different boundaries were used in the LPS (droplet model) and mPAP (periodic boundary) simulations, to ease the comparison, we have scaled the LPS RDF such that both curves have the same heights for the first peak. (B) Comparisons between mPAP results with different truncation orders of the many-body expansion of potential. The fifth-order curve is based on the 10 ps combined trajectories (the first 5 ps each) of Long₁ and Long₂. The fourth-order curve is based on the 10 ps combined trajectories of Add-b₁ and Add-b₂, the third-order curve on combined Add-b₃ and Add-b₄, and the second-order curve on combined Add-b₅ and Add-b₆. (C) Comparisons between mPAP results with different time step sizes, where the time step size and truncate order are indicated in parentheses. The (0.5 fs, fifth) curve is based on the 10 ps combined trajectories (the first 5 ps each) of Long₁ and Long₂, the (0.1 fs, fifth) curve on the 7 ps combined trajectories of Add-c₁ and Add-c₂, and the (0.1 fs, third) curve on the 10 ps combined trajectories of Add-c₃ and Add-c₄. (D) Comparisons between mPAP results with and without coupled thermostat. The curve with the coupled thermostat is based on the 10 ps combined trajectories (the first 5 ps each) of Long₁ and Long₂, and the curve without the thermostat is based on the 10 ps combined trajectories of Add-d₁ and Add-d₂.

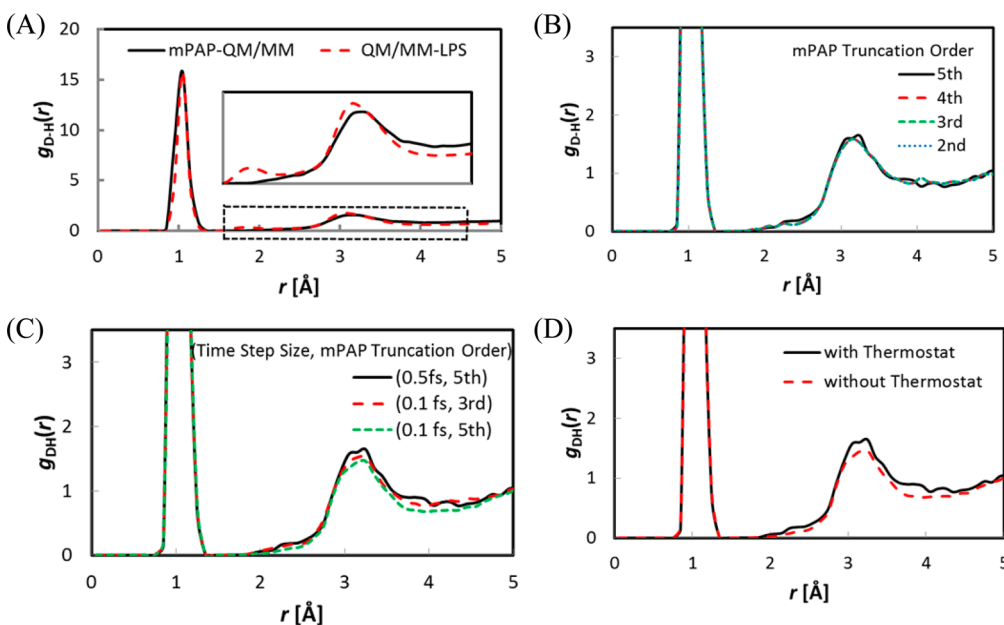


Figure 6. Same as Figure 5 except addressing the radial distribution function $g_{D-H}(r)$, where H is the hydrogen of water. The inset in panel (A) shows details of the section of $1.5 \text{ Å} \leq r \leq 4.5 \text{ Å}$.

may contribute to this difference, we suspect that the leading cause is the small size of the active-zone in the mPAP calculations. Note that only the water molecules within 4.0 Å of the proton indicator are QM, whereas the others are MM. This

means that donor D is only 2.8 Å away from MM water when the hydrated proton takes the Zundel-like structure. Because the QM and MM potentials for water–water interactions are aligned at $r \rightarrow \infty$ (for simplicity), they differ from each other

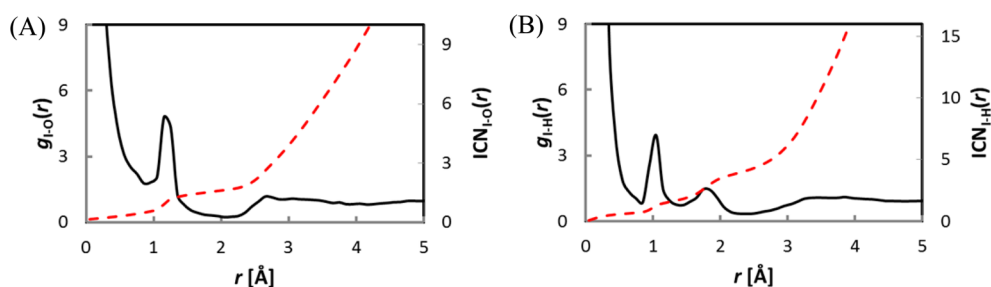


Figure 7. Radial distribution function (RDF) $g_{I-O}(r)$ and $g_{I-H}(r)$ in (A) and (B), respectively, where I is the proton indicator, O the oxygen of water, and H the hydrogen of water. Also plotted are the corresponding integrated coordination numbers (ICNs) as dashed curves. The results are based on the 45 ps combined trajectories of Long₁, Long₂ and Long₃.

when the water molecules are in close proximity. The mismatch of potentials would affect the water structures in the vicinity of the hydronium ion. In contrast, the QM/MM-LPS simulations saw the hydronium ion always stay within 5 Å of the origin of the QM subsystem, a sphere with a radius of 12 Å.⁴⁵ As a result, the donor was surrounded by QM water molecules of thickness always ≥ 7 Å and most of the time > 9 Å.⁴⁵ The different solvation environments for the donor in mPAP and LPS undoubtedly contributed to the differences in the $g_{D-O}(r)$ and $n_{D-O}(r)$ plots.

Next, we examined how different computational setups affected the computed solvation structure. As indicated by Figure 5 (B), truncation of the many-body expansion down to second order does not seem to significantly modify $g_{D-O}(r)$. This observation implies that, for the model system employed here, the high-order terms in the many-body expansion contribute insignificantly. In Figure 5 (C), the two curves (0.5 fs, fifth) and (0.1 fs, third) agree well with each other, both of which are based on 10 ps combined trajectories. The (0.1 fs, fifth) curve displays a peak that is slightly higher and narrower. The difference is probably caused by poorer statistics in the (0.1 fs, fifth) data due to the shorter 7 ps combined trajectories. However, the overall variations are minor, suggesting that a time step size of 0.5 fs is likely sufficient to yield a reasonably accurate RDF. Interestingly, Figure 5 (D) reveals very similar solvation structures of the hydrated proton in the simulations with and without a coupled thermostat. As we shall see in Section IV.D, both the temperature and energy increased slowly for the model system in the simulations without a thermostat due to the conservation of momentum and the utilization of many-body expansion potential in mPAP. Therefore, both the Add-d₁ and Add-d₂ simulations remained stable within the 5 ps simulation time and approximately sampled a microcanonical ensemble. Thus, we reason that the two $g_{D-O}(r)$ curves in Figure 5 (D) agree with each other because, at the thermodynamic limit, all ensembles should yield the same RDF. The ICN plots in Figure S1 (B–D) in the Supporting Information confirm the above conclusions based on the analysis of the RDFs. Again, we found that the (0.1 fs, fifth) curve in Figure S1 (C) in the Supporting Information varies slightly from the other two curves. As mentioned above, this is probably due to the use of shorter 7 ps combined trajectories for the (0.1 fs, fifth) plot.

The RDF $g_{D-H}(r)$ curves echo what we have observed in the $g_{D-O}(r)$ plots; here, H denotes water hydrogen. For example, the mPAP and LPS results are almost identical for $r < 1.5$ Å (Figure 6 (A)). Both display a sharp peak at $r = 1.0$ Å, which corresponds to the covalently bonded hydrogen atoms in the hydronium ion. As r increases, some minor discrepancies start

to show. In mPAP, the second peak is located at approximately $r = 3.2$ Å, which is due to the hydrogen atoms of water molecules in the first solvation shell of the hydrated proton (see the inlet in Figure 6 (A)). The location of the second peak moves slightly to $r = 3.1$ Å in the LPS plot. However, the small peak at $r = 1.8$ Å in the LPS plot was absent from the mPAP curve. Again, the variations in the truncation order, time step size, and thermostat employment do not significantly change the $g_{D-H}(r)$ curves, as indicated in Figure 6 (B–D). The conclusions are further confirmed by the ICN plots in Figure S2 in the Supporting Information.

Although the proton indicator is not a real atom, it is interesting to examine its “solvation structure”. Because the indicator superimposes with the hydronium oxygen in the Eigen-like structures and with the shared hydrogen in the Zundel-like structures, we expect that such a feature would be reflected in the RDFs. Figure 7 displays the RDFs $g_{I-O}(r)$ and $g_{I-H}(r)$ together with their corresponding ICNs, all calculated using the long trajectories Long₁, Long₂, and Long₃. Indeed, $g_{I-O}(r)$ monotonously increases rapidly when approaching $r = 0$, which corresponds to the hydronium oxygen in the Eigen-like structures. The peak near $r = 1.2$ Å arises from the oxygen in the Zundel-like geometries, where the proton indicator resides at the shared hydrogen in the middle of the two water molecules. In the $g_{I-H}(r)$ curve, the large value at $r = 0$ is due to the shared hydrogen in the Zundel-like geometries, the peak at $r = 1.1$ Å can be attributed to the hydronium hydrogen in the Eigen-like structures, and the peak at $r = 1.8$ Å represents the other four hydrogen atoms in the Zundel-like structures.

IV.C. Proton Hopping in Bulk Water. The location of the proton indicator is determined by the ratio ρ_{mij} which indicates how close H_m is to donor D versus to a possible acceptor A_j . Proton transfer is determined by the largest ρ_{mij} , denoted ρ , which identifies the most likely acceptor. As mentioned earlier, due to the use of finite step size, occasionally a ρ_{mij} may transiently go above 0.5. In such a case, the ρ_{mij} that is larger than 0.5 is the largest ρ_{mij} or ρ . A value larger than 0.5 for ρ means that the donor and acceptor should have switched if an even smaller step size were used; therefore, we took the complementary value $1 - \rho_{mij}$ for data analysis in such a case. As an example, Figure 8 displays ρ for the Long₁ sample trajectory versus simulation time. The value of ρ varies smoothly between 0.38 and 0.50 during the simulations.

On the basis of the probability distribution of ρ , in Figure 9, we computed and plotted the potential of mean force (PMF) using ρ as the reaction coordinate. Also plotted are the PMFs associated with the commonly used reaction ordinate $dr = |r_{DH'}| - |r_{AH'}|$, where H' is the hydrogen atom being transferred between donor D and acceptor A. Both reaction coordinates

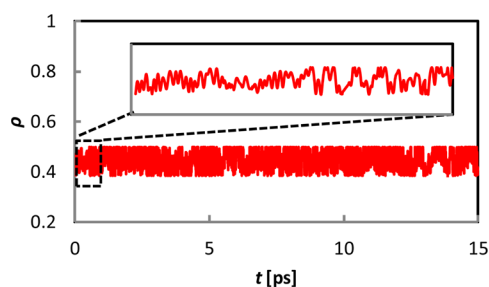


Figure 8. Ratio ρ as a function of simulation time for the sample trajectory Long₁. The inset shows ρ for the first 1 ps.

produce very similar PMFs, although usually the barrier is slightly lower in the PMF of dr than in the corresponding PMF

of ρ . Although the simulation times are probably not long enough to fully converge the PMFs, all plots except two (the third-order curves in Figure 9 (C and D)) indicate that the Eigen-structure is the resting state and that there is a small but finite free-energy barrier for proton transfer in qualitative agreement with the QM/MM-LPS simulations.⁴⁵ We were unable to determine why the third-order curves differ from the others, although we suspect that large statistical errors might be the reason. The mPAP barrier ranges from 0.05 to 0.19 kcal/mol when using ρ as the reaction coordinate and from 0.02 to 0.15 kcal/mol in the case of dr . For comparison, the corresponding LPS barriers were 0.19 for ρ and 0.06 kcal/mol for dr , respectively.⁴⁵ Although it is very challenging to determine the exact barrier height for such a small reaction barrier, our results are in line with the ab initio path integral

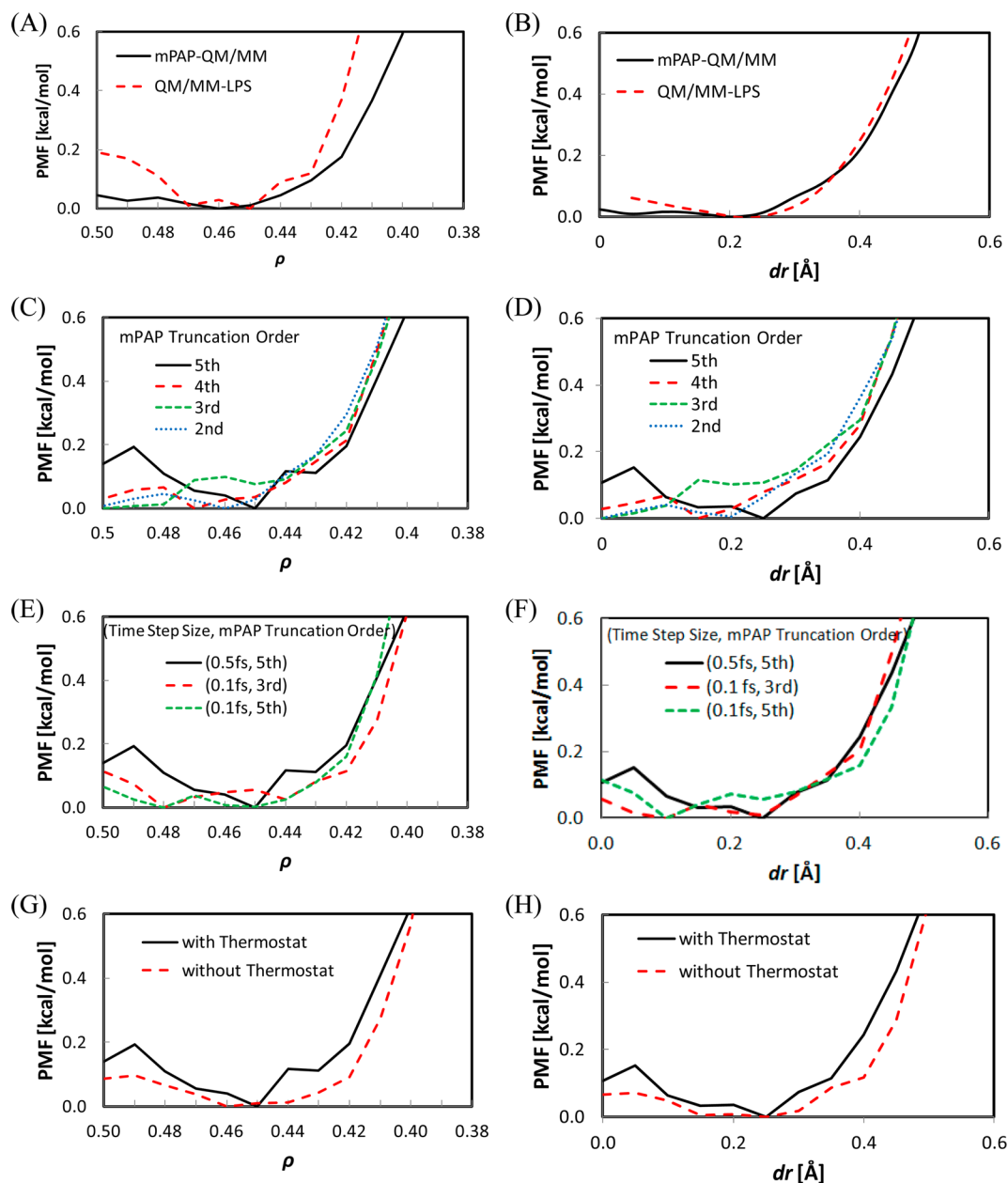


Figure 9. Potential of mean force (PMF) for proton transfer for reaction coordinates ρ in panels (A), (C), (E), and (G) and for reaction coordinate $dr = |\mathbf{r}_{\text{DH}}| - |\mathbf{r}_{\text{AH}}|$ in panels (B), (D), (F), and (H), where D is the donor, A the acceptor, and H' the hydrogen atom transferred between D and A. Refer to the Figure 5 caption for the labeling of the curves.

calculations (barrier of 0.15 kcal/mol), which include the quantum fluctuations of all nuclei.^{28,29}

The mPAP PMFs in Figure 9 (A and B) are presumed to be the most reliable because they are based on the longest (45 ps) combined trajectories of Long₁, Long₂, and Long₃. In agreement with the QM/MM-LPS results, the Zundel structure was found in the transition state and the Eigen structure in the resting state. The location of the resting state has been slightly shifted from $\rho = 0.45$ in LPS to $\rho = 0.46$ in mPAP (and from $dr = 0.25$ Å in LPS to $dr = 0.20$ Å in mPAP). The mPAP barrier heights (0.06 kcal/mol for ρ and 0.02 kcal/mol for dr) are lower than those by LPS (0.19 and 0.06 kcal/mol).⁴⁵ The discrepancies are likely caused by the mismatch of the QM and MM potentials near the QM/MM boundary described above. The mismatch of potential near the boundary ($r \sim 4$ Å) resulted in less water surrounding the hydronium ion, destabilizing the Eigen structure. As can be seen in Figure S1 (A) in the Supporting Information, there is a lower water density near the boundary of the QM region, indicating a decrease in the coordination number of the acceptor water molecule. It is generally accepted that a temporary decrease in acceptor coordination is the rate-limiting step in a forward hopping motion.² As such, the reduction in the acceptor coordination number stabilizes the transition state with respect to the reactant, lowering the barrier of proton transfer. Consequently, the hydrated proton takes more Zundel-like structures in the simulations. Overall, the mPAP and LPS data agree well with each other qualitatively in the descriptions of proton transfer in bulk water, but we have yet to achieve quantitative agreement in the free-energy barrier heights.

In Figure 10, we plot the root-mean-square deviations (RMSD) of the donor and of the indicator versus simulation time with respect to their initial positions for the Add-a₁ and

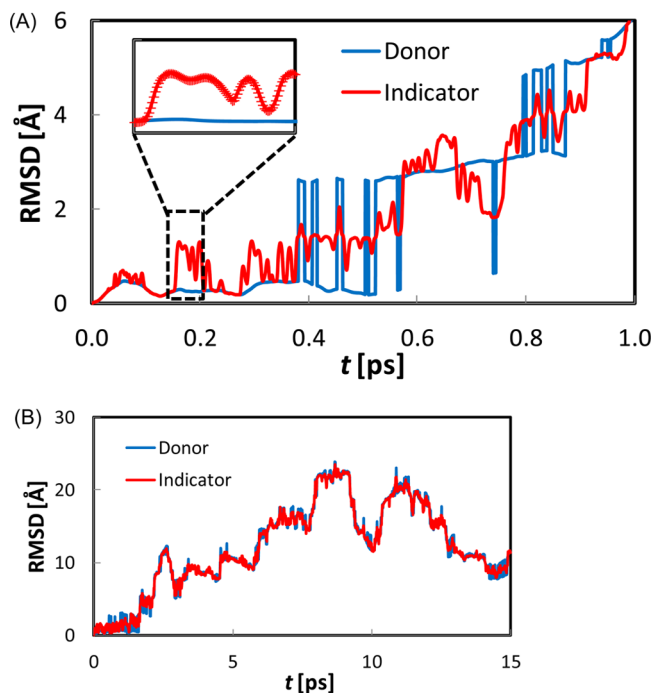


Figure 10. Root mean square deviation (RMSD) as a function of simulation time with respect to the initial positions for the donor and the proton indicator in (A) the short trajectory Add-a₁ and (B) the long trajectory Long₁.

Long₁ sample trajectories. It can be seen that the evolutions of the RMSD for the donor and for the indicator are in line with each other with the indicator generally having smaller fluctuations. A prominent feature in the donor's plot is clusters of vertical lines (e.g., those between $t = 0.4$ and 0.6 ps in the Add-a₁ plot). These vertical lines correspond to the Zundel-like structures, where donor and acceptor exchange status frequently, with the sudden variations leading to abrupt changes in the RMSD value of the donor. During this period, the indicator was typically located between the donor and acceptor, as reflected by the smoothly changing RMSD curve of the indicator that lies near the middle of the vertical lines. On the other hand, the RMSD value of the indicator varied quickly whereas the donor's plot was almost level (e.g., between $t = 0.15$ and 0.20 ps in the Add-a₁ trajectory). This is because the indicator was wandering around whereas the donor stayed at the hydronium oxygen. However, the variations in the indicator position were smooth (see the inset in Figure 10 (A)), preventing abrupt changes to the active zone. The conclusion is further confirmed by analyzing the RMSD plots for other trajectories (e.g., those for Add-c₁ and Add-d₅ in Figure S3 in the Supporting Information).

IV.D. Numerical Stability of the mPAP Scheme. The mPAP scheme describes a non-Hamiltonian system because the forces due to smoothing functions are deleted. The treatment is equivalent to having external forces acting on the system cancel those forces due to smoothing functions. As a result, the energy is no longer conserved, and the system will be heated over time in the mPAP simulations. This is demonstrated by the Add-d₁ and Add-d₂ simulations, where no thermostat was coupled to the model system. Figure 11 plots the energies and temperatures as functions of simulation time for Add-d₁ and Add-d₂. Both the energy and temperature increased almost linearly during a simulation. The energies increased by approximately 350 and 380 kcal/mol per ps for Add-d₁ and Add-d₂,

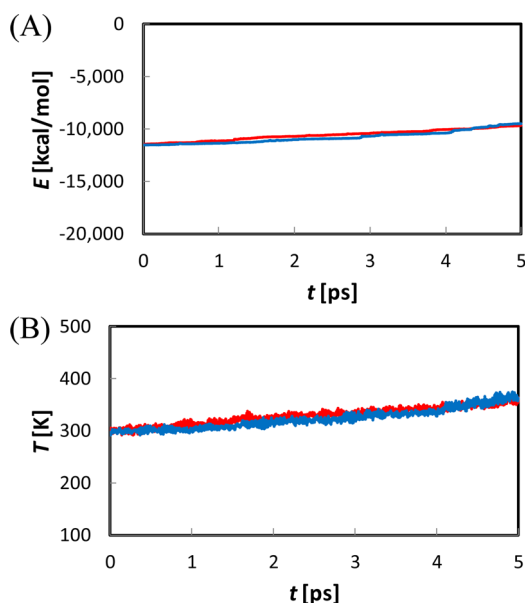


Figure 11. (A) Total energy and (B) temperature as functions of simulation time for the Add-d₁ (red) and Add-d₂ (blue) calculations. Neither calculation employs a thermostat. Linear regression of the four sets of data yielded coefficients of determination (R^2) in the range of 0.92 to 0.99.

respectively, leading to increases in energy of ~ 1800 kcal/mol at the end of the 5 ps simulations. The temperatures grew by 12 K per ps, causing an elevation by ~ 60 K after 5 ps. For comparison, we note that the other adaptive schemes yielded similar or larger average temperature drifting rates in a recent test of “QM water solvated in MM water” by Buló et al.⁸¹ For example, in the simulations with a water box of 15 Å, when a semiempirical QM Hamiltonian (PM6-DH+^{41,93}) and a nonreactive MM water model (TIP3P-Fs⁹⁴) were employed for a spherical active-zone of 4 Å radius, the average temperature drifting rates are 29 K/ps for the difference-based adaptive solvation (DAS) scheme, 250 K/ps for the sorted adaptive partitioning (SAP) scheme, and 630 K/ps for the buffered force (BF) scheme.⁸¹ The DAS simulations with a larger box of 30 Å at the level of DFTB⁹⁵ and TIP3P-Fs combination yielded a drift in the temperature of 7.2 K/ps.⁸¹ The smaller average temperature drifting rate of 12 K/ps obtained by mPAP from proton hopping simulations demonstrates the excellent numerical stability of the mPAP scheme.

V. DISCUSSION

A significant advantage of adaptive QM/MM simulations is the employment of a small QM subsystem whose location and contents are continuously updated automatically on-the-fly. The challenge in adaptive QM/MM simulations of proton solvated in bulk water is the fact that it is the structural features (the covalent and hydrogen bonding network) instead of the given proton that is being transferred via the Grotthuss hopping mechanism. Therefore, it is crucial to identify an appropriate reference point for the active-zone center so that the active zone can follow the structural variation smoothly. The results presented above demonstrate that the proton indicator serves well as the active-zone center in mPAP-QM/MM simulations, avoiding abrupt changes in the location and contents of the active zone, which is critical to the success of the MD simulations. Reasonably good agreements have been achieved in the proton solvation structure and in the proton transfer dynamics between mPAP with a small active zone of radius $R_{\min} = 4$ Å and the conventional QM/MM-LPS simulations with a much larger spherical QM subsystem of radius $R = 12$ Å,⁴⁵ which are of comparable computational costs (Table S2 in the Supporting Information). We also found that the performances of the mPAP and proton indicator in the test calculations were not sensitive to the utilized time step size (0.5 or 0.1 fs), truncation order (fifth to second) of the many-body expansion of potential, and even the presence or absence of a thermostat. The results suggest that mPAP equipped with the proton indicator can be useful to study a hydrated proton in water. In principle, the proton indicator can also be applied to other adaptive QM/MM implementations.

Although the reasonable agreements between mPAP and LPS are encouraging, differences have been observed in the proton solvation structures and in the PMF of proton transfer. For example, the barriers for proton transfer by mPAP are lower than those by LPS. A lower barrier may lead to overestimation of proton hopping rate. Indeed, the forward hopping rate (defined in the same way as in ref 45, see also the Supporting Information) was computed to be 5.4 ps^{-1} on the basis of the three long trajectories Long₁, Long₂, and Long₃. The result is much larger than the 0.53 ps^{-1} by LPS,⁴⁵ which is close to the 0.71 ps^{-1} experimental value.²² As pointed out earlier, the differences between the mPAP and LPS results are

most likely due to the different interactions between the water molecules in the first solvation shell of the hydrated proton and the water molecules immediately surrounding the first solvation shell. These interactions were described at the QM level in LPS but were treated at the MM level in the mPAP test calculations, where the mechanical embedding scheme has been adopted for simplicity. The mechanical embedding scheme suffices for the purpose of the present study (i.e., to demonstrate the feasibility of the proton indicator acting as the active-zone center in adaptive QM/MM). However, a side effect is the mismatch of the QM and MM potentials in the region very close to the hydrated proton. We believe that this potential mismatch is the primary negative impact on the mPAP performance.

In principle, one can reparameterize the QM and MM potentials or align them such that they agree with each other at the QM/MM boundary. This will eliminate the potential mismatch and should improve the results. However, this is very challenging to accomplish because of the multidimensional nature of the potentials. To our knowledge, there is no easy way to do the required reparameterization or alignment. Future research is needed to develop simple and general approaches for potential matching.

Another solution is to adopt a larger active zone, which will push the QM/MM boundary further away from the hydrated proton and thus diminish the effects due to potential mismatch. Given that the QM/MM-LPS simulations had employed a spherical QM subsystem of radius $R = 12$ Å, it is conceivable that the mPAP results will converge toward the LPS results if the active-zone radius increases gradually to 12 Å. Unfortunately, we were unable to numerically verify this in the present contribution because the Add-e set of test calculations ($R_{\min} = 6$ and 8 Å) were computationally too expensive to generate sufficiently long trajectories for reliable analysis, as indicated in Table S2 in the Supporting Information. This task will have to be addressed in a future study. (It should be pointed out that the computational costs can be reduced by using the SAP or DAS scheme, where the number of QM calculations at each time step scales linearly with the number of buffer groups. However, the SAP and DAS schemes are numerically not as stable as PAP or mPAP, and more work is required before the SAP and DAS test calculations can begin.)

If the goal is to keep the size of the QM subsystem small, it is worth trying more advanced QM/MM embedding schemes, where the electrostatic interactions between the QM and MM atoms are computed through effective QM/MM Hamiltonians instead of by Coulomb's Law using point charges at the MM level.^{63,68} Although more advanced QM/MM embedding schemes are unlikely to eliminate the potential mismatch, they may alleviate the problem. Some examples of more sophisticated and presumably more accurate embedding schemes include the electrostatic embedding scheme,^{96,97} which accounts for the polarization of the QM subsystem by the MM subsystem, the polarized-boundary embedding scheme,⁹⁸ which describes mutual polarization between the QM and MM subsystems, and the flexible-boundary embedding scheme,^{99–101} which treats both the mutual polarization and partial charge transfer between the QM and MM subsystems. Because of the significant charge of the hydronium ion, charge delocalization is likely over the water molecules surrounding the hydrated proton and may extend beyond the first solvation shell. Moreover, how the charge is exactly delocalized probably changes dynamically along with the proton hopping as the network of covalent and hydrogen

bonds is reorganized on-the-fly.^{36,101–105} Therefore, it would be intriguing to compare the mPAP results computed with systematically improved embedding schemes in the future.

■ ASSOCIATED CONTENT

● Supporting Information

Additional details about gradient calculations for the proton indicator, three different weight functions that have been tested, an accumulation function for forward proton hops, a list of all test calculations (Table S1), a list of computational times for selected jobs (Table S2), integrated coordination numbers for donor and water oxygen (Figure S1) and for donor and water hydrogen (Figure S2), root-mean-square deviation as a function of simulation time for trajectories Add-b₅ and Add-c₁ (Figure S3), forward hops of the excess proton in the Add-a₁ and Long₁ trajectories (Figure S4), and a movie for the Add-a₁ sample trajectory. The Supporting Information is available free of charge on the ACS Publications website at DOI: 10.1021/ct501019y.

■ AUTHOR INFORMATION

Corresponding Author

*E-mail: hai.lin@ucdenver.edu. Phone: 303-352-3889. Fax: 303-556-4776.

Notes

The authors declare no competing financial interest.

■ ACKNOWLEDGMENTS

This work is supported by the National Science Foundation (CHE-0952337). This work used the Extreme Science and Engineering Discovery Environment (XSEDE) under Grant CHE-140070, which is supported by National Science Foundation Grant ACI-1053575. H.L. thanks the Camille & Henry Dreyfus Foundation for support (TH-14-028). We thank Adam Duster for critical reading of the manuscript.

■ REFERENCES

- (1) Agmon, N. The Grotthuss mechanism. *Chem. Phys. Lett.* **1995**, 244, 456–462.
- (2) Marx, D. Proton transfer 200 years after von Grotthuss: Insights from ab initio simulations. *ChemPhysChem* **2006**, 7, 1848–1870.
- (3) Stillinger, F. H.; David, C. W. Polarization model for water and its ionic dissociation products. *J. Chem. Phys.* **1978**, 69, 1473–1484.
- (4) David, C. W. A variable charge central force model for water and its ionic dissociation products. *J. Chem. Phys.* **1996**, 104, 7255–7260.
- (5) Halley, J. W.; Rustad, J. R.; Rahman, A. A polarizable, dissociating molecular dynamics model for liquid water. *J. Chem. Phys.* **1993**, 98, 4110–4119.
- (6) Billeter, S. R.; van Gunsteren, W. F. Protonizable water model for quantum dynamical simulations. *J. Phys. Chem. A* **1998**, 102, 4669–4678.
- (7) Lussetti, E.; Pastore, G.; Smargiassi, E. A fully polarizable and dissociable potential for water. *Chem. Phys. Lett.* **2003**, 381, 287–291.
- (8) Mahadevan, T. S.; Garofalini, S. H. Dissociative water potential for molecular dynamics simulations. *J. Phys. Chem. B* **2007**, 111, 8919–8927.
- (9) Fogarty, J. C.; Aktulga, H. M.; Grama, A. Y.; van Duin, A. C. T.; Pandit, S. A. A reactive molecular dynamics simulation of the silica-water interface. *J. Chem. Phys.* **2010**, 132, 174704/1–14.
- (10) Selvan, M. E.; Keffer, D. J.; Cui, S.; Paddison, S. J. A reactive molecular dynamics algorithm for proton transport in aqueous systems. *J. Phys. Chem. C* **2010**, 114, 11965–11976.
- (11) Kale, S.; Herzfeld, J.; Dai, S.; Blank, M. Lewis-inspired representation of dissociable water in clusters and Grotthuss chains. *J. Biol. Phys.* **2012**, 38, 49–59.
- (12) Wolf, M. G.; Groenhof, G. Explicit proton transfer in classical molecular dynamics simulations. *J. Comput. Chem.* **2014**, 35, 657–671.
- (13) Sagnella, D. E.; Tuckerman, M. E. An empirical valence bond model for proton transfer in water. *J. Chem. Phys.* **1998**, 108, 2073/1–11.
- (14) Schmitt, U. W.; Voth, G. A. Multistate empirical valence bond model for proton transport in water. *J. Phys. Chem. B* **1998**, 102, 5547–5551.
- (15) Vuilleumier, R.; Borgis, D. An extended empirical valence bond model for describing proton transfer in H⁺(H₂O)_n clusters and liquid water. *Chem. Phys. Lett.* **1998**, 284, 71–77.
- (16) Vuilleumier, R.; Borgis, D. Transport and spectroscopy of the hydrated proton: A molecular dynamics study. *J. Chem. Phys.* **1999**, 111, 4251–4266.
- (17) Lefohn, A. E.; Ovchinnikov, M.; Voth, G. A. A multistate empirical valence bond approach to a polarizable and flexible water model. *J. Phys. Chem. B* **2001**, 105, 6628–6637.
- (18) Kornyshev, A. A.; Kuznetsov, A. M.; Spohr, E.; Ulstrup, J. Kinetics of proton transport in water. *J. Phys. Chem. B* **2003**, 107, 3351–3366.
- (19) Brancato, G.; Tuckerman, M. E. A polarizable multistate empirical valence bond model for proton transport in aqueous solution. *J. Chem. Phys.* **2005**, 122, 224507/1–11.
- (20) Swanson, J. M. J.; Maupin, C. M.; Chen, H.; Petersen, M. K.; Xu, J.; Wu, Y.; Voth, G. A. Proton solvation and transport in aqueous and biomolecular systems: Insights from computer simulations. *J. Phys. Chem. B* **2007**, 111, 4300–4314.
- (21) Markovitch, O.; Chen, H.; Izvekov, S.; Paesani, F.; Voth, G. A.; Agmon, N. Special pair dance and partner selection: Elementary steps in proton transport in liquid water. *J. Phys. Chem. B* **2008**, 112, 9456–9466.
- (22) Wu, Y. J.; Chen, H. N.; Wang, F.; Paesani, F.; Voth, G. A. An improved multistate empirical valence bond model for aqueous proton solvation and transport. *J. Phys. Chem. B* **2008**, 112, 467–482.
- (23) Park, K.; Lin, W.; Paesani, F. A refined MS-EVB model for proton transport in aqueous environments. *J. Phys. Chem. B* **2012**, 116, 343–352.
- (24) Cao, Z.; Kumar, R.; Peng, Y.; Voth, G. A. Proton transport under external applied voltage. *J. Phys. Chem. B* **2014**, 118, 8090–8098.
- (25) Park, K.; Lin, W.; Paesani, F. Fast and slow proton transfer in ice: The role of the quasi-liquid layer and hydrogen-bond network. *J. Phys. Chem. B* **2014**, 118, 8081–8089.
- (26) Tuckerman, M. E.; Laasonen, K.; Sprik, M.; Parrinello, M. Ab initio simulations of water and water ions. *J. Phys.: Condens. Matter* **1994**, 6, A93–A100.
- (27) Tuckerman, M.; Laasonen, K.; Sprik, M.; Parrinello, M. Ab initio molecular dynamics simulation of the solvation and transport of H₃O⁺ and OH[−] Ions in Water. *J. Phys. Chem.* **1995**, 99, 5749–5752.
- (28) Marx, D.; Tuckerman, M. E.; Hutter, J.; Parrinello, M. The nature of the hydrated excess proton in water. *Nature* **1999**, 397, 601–604.
- (29) Marx, D.; Tuckerman, M. E.; Parrinello, M. Solvated excess protons in water: quantum effects on the hydration structure. *J. Phys.: Condens. Matter* **2000**, 12, A153–A159.
- (30) Asthagiri, D.; Pratt, L. R.; Kress, J. D. Ab initio molecular dynamics and quasichemical study of H⁺(aq). *Proc. Natl. Acad. Sci. U.S.A.* **2005**, 102, 6704–6708.
- (31) Chandra, A.; Tuckerman, M. E.; Marx, D. Connecting solvation shell structure to proton transport kinetics in hydrogen-bonded networks via population correlation functions. *Phys. Rev. Lett.* **2007**, 99, 145901/1–4.
- (32) Berkelbach, T. C.; Lee, H.-S.; Tuckerman, M. E. Concerted hydrogen-bond dynamics in the transport mechanism of the hydrated proton: A first-principles molecular dynamics study. *Phys. Rev. Lett.* **2009**, 103, 238302/1–4.
- (33) Swanson, J. M. J.; Simons, J. Role of charge transfer in the structure and dynamics of the hydrated proton. *J. Phys. Chem. B* **2009**, 113, 5149–5161.

- (34) Tuckerman, M. E.; Chandra, A.; Marx, D. A statistical mechanical theory of proton transport kinetics in hydrogen-bonded networks based on population correlation functions with applications to acids and bases. *J. Chem. Phys.* **2010**, *133*, 124108/1–22.
- (35) Marsalek, O.; Elles, C. G.; Pieniazek, P. A.; Pluharova, E.; VandeVondele, J.; Bradforth, S. E.; Jungwirth, P. Chasing charge localization and chemical reactivity following photoionization in liquid water. *J. Chem. Phys.* **2011**, *135*, 224510/1–14.
- (36) Giberti, F.; Hassanali, A. A.; Ceriotti, M.; Parrinello, M. The role of quantum effects on structural and electronic fluctuations in neat and charged water. *J. Phys. Chem. B* **2014**, *118*, 13226–13235.
- (37) Car, R.; Parrinello, M. Unified approach for molecular dynamics and density-functional theory. *Phys. Rev. Lett.* **1985**, *55*, 2471–2474.
- (38) Riccardi, D.; König, P.; Prat-Resina, X.; Yu, H. B.; Elstner, M.; Frauenheim, T.; Cui, Q. “Proton holes” in long-range proton transfer reactions in solution and enzymes: A theoretical analysis. *J. Am. Chem. Soc.* **2006**, *128*, 16302–16311.
- (39) Arillo-Flores, O. I.; Ruiz-López, M. F.; Bernal-Uruchurtu, M. I. Can semi-empirical models describe HCl dissociation in water? *Theor. Chem. Acc.* **2007**, *118*, 425–435.
- (40) Choi, T. H.; Jordan, K. D. Application of the SCC-DFTB method to $\text{H}^+(\text{H}_2\text{O})_6$, $\text{H}^+(\text{H}_2\text{O})_{21}$, and $\text{H}^+(\text{H}_2\text{O})_{22}$. *J. Phys. Chem. B* **2010**, *114*, 6932–6936.
- (41) Korth, M. Third-generation hydrogen-bonding corrections for semiempirical QM methods and force fields. *J. Chem. Theory Comput.* **2010**, *6*, 3808–3816.
- (42) Maupin, C. M.; Aradi, B. I.; Voth, G. A. The self-consistent charge density functional tight binding method applied to liquid water and the hydrated excess proton: Benchmark simulations. *J. Phys. Chem. B* **2010**, *114*, 6922–6931.
- (43) Goyal, P.; Elstner, M.; Cui, Q. Application of the SCC-DFTB method to neutral and protonated water clusters and bulk water. *J. Phys. Chem. B* **2011**, *115*, 6790–6805.
- (44) Lin, Y.; Wynveen, A.; Halley, J. W.; Curtiss, L. A.; Redfern, P. C. Self consistent tight binding model for dissociable water. *J. Chem. Phys.* **2012**, *136*, 174507/1–12.
- (45) Wu, X.; Thiel, W.; Pezeshki, S.; Lin, H. Specific reaction path Hamiltonian for proton transfer in water: Reparameterized semi-empirical models. *J. Chem. Theory Comput.* **2013**, *9*, 2672–2686.
- (46) Goyal, P.; Qian, H.-J.; Irle, S.; Lu, X.; Roston, D.; Mori, T.; Elstner, M.; Cui, Q. Molecular simulation of water and hydration effects in different environments: Challenges and developments for DFTB based models. *J. Phys. Chem. B* **2014**, *118*, 11007–11027.
- (47) Wang, S.; MacKay, L.; Lamoureux, G. Development of semiempirical models for proton transfer reactions in water. *J. Chem. Theory Comput.* **2014**, *10*, 2881–2890.
- (48) Warshel, A.; Levitt, M. Theoretical studies of enzymic reactions: Dielectric, electrostatic and steric stabilization of the carbonium ion in the reaction of lysozyme. *J. Mol. Biol.* **1976**, *103*, 227–249.
- (49) Singh, U. C.; Kollmann, P. A. A combined ab initio quantum mechanical and molecular mechanical method for carrying out simulations on complex molecular systems: Applications to the $\text{CH}_3\text{Cl} + \text{Cl}^-$ exchange reaction and gas phase protonation of polyethers. *J. Comput. Chem.* **1986**, *7*, 718–730.
- (50) Field, M. J.; Bash, P. A.; Karplus, M. A combined quantum mechanical and molecular mechanical potential for molecular dynamics simulations. *J. Comput. Chem.* **1990**, *11*, 700–733.
- (51) Gao, J. Methods and applications of combined quantum mechanical and molecular mechanical potentials. *Rev. Comput. Chem.* **1996**, *7*, 119–185.
- (52) Friesner, R. A.; Beachy, M. D. Quantum mechanical calculations on biological systems. *Curr. Opin. Struct. Biol.* **1998**, *8*, 257–262.
- (53) Gao, J.; Thompson, M. A., Eds. *Combined quantum mechanical and molecular mechanical methods*; ACS Symp. Ser. 712; American Chemical Society: Washington, DC, 1998; p 310.
- (54) Ruiz-López, M. F.; Rivail, J. L. Combined quantum mechanics and molecular mechanics approaches to chemical and biochemical reactivity. In *Encyclopedia of computational chemistry*, von Ragué Schleyer, P., Ed.; Wiley: Chichester, 1998; Vol. 1, pp 437–448.
- (55) Monard, G.; Merz, K. M., Jr. Combined quantum mechanical/molecular mechanical methodologies applied to biomolecular systems. *Acc. Chem. Res.* **1999**, *32*, 904–911.
- (56) Hillier, I. H. Chemical reactivity studied by hybrid QM/MM methods. *J. Mol. Struct.: THEOCHEM* **1999**, *463*, 45–52.
- (57) Hammes-Schiffer, S. Theoretical perspectives on proton-coupled electron transfer reactions. *Acc. Chem. Res.* **2000**, *34*, 273–281.
- (58) Sherwood, P. Hybrid quantum mechanics/molecular mechanics approaches. In *Modern Methods and Algorithms of Quantum Chemistry*; Grotendorst, J., Ed.; John von Neumann-Institut: Jülich, Germany, 2000; Vol. 3, pp 285–305.
- (59) Gao, J.; Truhlar, D. G. Quantum mechanical methods for enzyme kinetics. *Annu. Rev. Phys. Chem.* **2002**, *53*, 467–505.
- (60) Morokuma, K. New challenges in quantum chemistry: quests for accurate calculations for large molecular systems. *Philos. Trans. R. Soc., A* **2002**, *360*, 1149–1164.
- (61) Riccardi, D.; Schaefer, P.; Yang, Y.; Yu, H.; Ghosh, N.; Prat-Resina, X.; König, P.; Li, G.; Xu, D.; Guo, H.; Elstner, M.; Cui, Q. Development of effective quantum mechanical/molecular mechanical (QM/MM) methods for complex biological process. *J. Phys. Chem. B* **2006**, *110*, 6458–6469.
- (62) Zhang, Y. Pseudobond ab initio QM/MM approach and its applications to enzyme reactions. *Theor. Chem. Acc.* **2006**, *116*, 43–50.
- (63) Lin, H.; Truhlar, D. G. QM/MM: What have we learned, where are we, and where do we go from here? *Theor. Chem. Acc.* **2007**, *117*, 185–199.
- (64) Senn, H. M.; Thiel, W. QM/MM methods for biological systems. *Top. Curr. Chem.* **2007**, *268*, 173–290.
- (65) Hu, H.; Yang, W. Free energies of chemical reactions in solution and in enzymes with ab initio quantum mechanics/molecular mechanics methods. *Annu. Rev. Phys. Chem.* **2008**, *59*, 573–601.
- (66) Woodcock, H. L.; Miller, B. T.; Hodoscek, M.; Okur, A.; Larkin, J. D.; Ponder, J. W.; Brooks, B. R. MSCALC: A general utility for multiscale modeling. *J. Chem. Theory Comput.* **2011**, *7*, 1208–1219.
- (67) van der Kamp, M. W.; Mulholland, A. J. Combined quantum mechanics/molecular mechanics (QM/MM) methods in computational enzymology. *Biochemistry* **2013**, *52*, 2708–2728.
- (68) Pezeshki, S.; Lin, H. Recent developments in QM/MM methods towards open-boundary multi-scale simulations. *Mol. Simul.* **2014**, *41*, 168–189.
- (69) Kerdcharoen, T.; Liedl, K. R.; Rode, B. M. A QM/MM simulation method applied to the solution of Li^+ in liquid ammonia. *Chem. Phys.* **1996**, *211*, 313–323.
- (70) Kerdcharoen, T.; Morokuma, K. ONIOM-XS: an extension of the ONIOM method for molecular simulation in condensed phase. *Chem. Phys. Lett.* **2002**, *355*, 257–262.
- (71) Kerdcharoen, T.; Morokuma, K. Combined quantum mechanics and molecular mechanics simulation of Ca^{2+} /ammonia solution based on the ONIOM-XS method: Octahedral coordination and implication to biology. *J. Chem. Phys.* **2003**, *118*, 8856–8862.
- (72) Heyden, A.; Lin, H.; Truhlar, D. G. Adaptive partitioning in combined quantum mechanical and molecular mechanical calculations of potential energy functions for multiscale simulations. *J. Phys. Chem. B* **2007**, *111*, 2231–2241.
- (73) Buló, R. E.; Ensing, B.; Sikkema, J.; Visscher, L. Toward a practical method for adaptive QM/MM simulations. *J. Chem. Theory Comput.* **2009**, *5*, 2212–2221.
- (74) Guthrie, M. G.; Daigle, A. D.; Salazar, M. R. Properties of a method for performing adaptive, multilevel QM simulations of complex chemical reactions in the gas-phase. *J. Chem. Theory Comput.* **2010**, *6*, 18–25.
- (75) Nielsen, S. O.; Buló, R. E.; Moore, P. B.; Ensing, B. Recent progress in adaptive multiscale molecular dynamics simulations of soft matter. *Phys. Chem. Chem. Phys.* **2010**, *12*, 12401–12414.
- (76) Poma, A. B.; Delle Site, L. Classical to path-integral adaptive resolution in molecular simulation: Towards a smooth quantum-classical coupling. *Phys. Rev. Lett.* **2010**, *104*, 250201/1–4.

- (77) Pezeshki, S.; Lin, H. Adaptive-partitioning redistributed charge and dipole schemes for QM/MM dynamics simulations: On-the-fly relocation of boundaries that pass through covalent bonds. *J. Chem. Theory Comput.* **2011**, *7*, 3625–3634.
- (78) Bernstein, N.; Varnai, C.; Solt, I.; Winfield, S. A.; Payne, M. C.; Simon, I.; Fuxreiter, M.; Csanyi, G. QM/MM simulation of liquid water with an adaptive quantum region. *Phys. Chem. Chem. Phys.* **2012**, *14*, 646–656.
- (79) Park, K.; Gotz, A. W.; Walker, R. C.; Paesani, F. Application of adaptive QM/MM methods to molecular dynamics simulations of aqueous systems. *J. Chem. Theory Comput.* **2012**, *8*, 2868–2877.
- (80) Takenaka, N.; Kitamura, Y.; Koyano, Y.; Nagaoka, M. The number-adaptive multiscale QM/MM molecular dynamics simulation: Application to liquid water. *Chem. Phys. Lett.* **2012**, *524*, 56–61.
- (81) Buló, R. E.; Michel, C.; Fleurat-Lessard, P.; Sautet, P. Multiscale modeling of chemistry in water: Are we there yet? *J. Chem. Theory Comput.* **2013**, *9*, 5567–5577.
- (82) Várnai, C.; Bernstein, N.; Mones, L.; Csányi, G. Tests of an adaptive QM/MM calculation on free energy profiles of chemical reactions in solution. *J. Phys. Chem. B* **2013**, *117*, 12202–12211.
- (83) Watanabe, H. C.; Kubař, T.; Elstner, M. Size-consistent multipartitioning QM/MM: A stable and efficient adaptive QM/MM method. *J. Chem. Theory Comput.* **2014**, *10*, 4242–4252.
- (84) Pezeshki, S.; Davis, C.; Heyden, A.; Lin, H. Adaptive-partitioning QM/MM dynamics simulations: 3. Solvent molecules entering and leaving protein binding sites. *J. Chem. Theory Comput.* **2014**, *10*, 4765–4776.
- (85) Waller, M. P.; Kumbhar, S.; Yang, J. A density-based adaptive quantum mechanical/molecular mechanical method. *ChemPhysChem* **2014**, *15*, 3218–3225.
- (86) Mones, L.; Jones, A.; Götz, A. W.; Laino, T.; Walker, R. C.; Leimkuhler, B.; Csányi, G.; Bernstein, N. The adaptive buffered force QM/MM method in the CP2K and AMBER software packages. *J. Comput. Chem.* **2015**, *36*, 633–648.
- (87) Hofer, T. S.; Hitznerberger, M.; Randolf, B. R. Combining a dissociative water model with a hybrid QM/MM approach—a simulation strategy for the study of proton transfer reactions in solution. *J. Chem. Theory Comput.* **2012**, *8*, 3586–3595.
- (88) Jorgensen, W. L.; Chandrasekhar, J.; Madura, J. D.; Impey, R. W.; Klein, M. L. Comparison of simple potential functions for simulating liquid water. *J. Chem. Phys.* **1983**, *79*, 926–935.
- (89) Berendsen, H. J. C.; Postma, J. P. M.; van Gunsteren, W. F.; DiNola, A.; Haak, J. R. Molecular dynamics with coupling to an external bath. *J. Chem. Phys.* **1984**, *81*, 3684–3690.
- (90) Lin, H.; Zhang, Y.; Pezeshki, S.; Truhlar, D. G. *QMMM*, version 2.0.0.CO; University of Minnesota: Minneapolis, MN, 2015.
- (91) Ponder, J. W. *TINKER*, version 5.1; Washington University: St. Louis, MO, 2010.
- (92) Thiel, W. *MNDO2005*, version 7.0; Max-Planck-Institut für Kohlenforschung: Mülheim an der Ruhr, Germany, 2005.
- (93) Stewart, J. P. Optimization of parameters for semiempirical methods V: Modification of NDDO approximations and application to 70 elements. *J. Mol. Model.* **2007**, *13*, 1173–1213.
- (94) Wu, Y.; Tepper, H. L.; Voth, G. A. Flexible simple point-charge water model with improved liquid-state properties. *J. Chem. Phys.* **2006**, *124*, 024503/1–12.
- (95) Elstner, M.; Porezag, D.; Jungnickel, G.; Elsner, J.; Haugk, M.; Frauenheim, T.; Suhai, S.; Seifert, G. Self-consistent-charge density-functional tight-binding method for simulations of complex materials properties. *Phys. Rev. B* **1998**, *58*, 7260–7268.
- (96) Bakowies, D.; Thiel, W. Hybrid models for combined quantum mechanical and molecular mechanical approaches. *J. Phys. Chem.* **1996**, *100*, 10580–10594.
- (97) Lin, H.; Truhlar, D. G. Redistributed charge and dipole schemes for combined quantum mechanical and molecular mechanical calculations. *J. Phys. Chem. A* **2005**, *109*, 3991–4004.
- (98) Zhang, Y.; Lin, H.; Truhlar, D. G. Self-consistent polarization of the boundary in the redistributed charge and dipole scheme for combined quantum-mechanical and molecular-mechanical calculations. *J. Chem. Theory Comput.* **2007**, *3*, 1378–1398.
- (99) Zhang, Y.; Lin, H. Flexible-boundary quantum-mechanical/molecular-mechanical calculations: Partial charge transfer between the quantum-mechanical and molecular-mechanical subsystems. *J. Chem. Theory Comput.* **2008**, *4*, 414–425.
- (100) Zhang, Y.; Lin, H. Flexible-boundary QM/MM calculations: II. Partial charge transfer across the QM/MM boundary that passes through a covalent bond. *Theor. Chem. Acc.* **2010**, *126*, 315–322.
- (101) Pezeshki, S.; Lin, H. Molecular dynamics simulations of ion solvation by flexible-boundary QM/MM: On-the-fly partial charge transfer between QM and MM subsystems. *J. Comput. Chem.* **2014**, *35*, 1778–1788.
- (102) Zhao, Z.; Rogers, D. M.; Beck, T. L. Polarization and charge transfer in the hydration of chloride ions. *J. Chem. Phys.* **2010**, *132*, 014502/1–10.
- (103) Soniat, M.; Rick, S. W. The effects of charge transfer on the aqueous solvation of ions. *J. Chem. Phys.* **2012**, *137*, 044511/1–9.
- (104) Kumar, R.; Knight, C.; Wick, C. D.; Chen, B. Bringing reactivity to the aggregation-volume-bias Monte Carlo based simulation framework: Water nucleation induced by a reactive proton. *J. Phys. Chem. B* **2014**, DOI: 10.1021/jp508749x.
- (105) Soniat, M.; Rick, S. W. Charge transfer effects of ions at the liquid water/vapor interface. *J. Chem. Phys.* **2014**, *140*, 184703/1–10.